JGR Planets

RESEARCH ARTICLE
10.1029/2024JE008466

Key Points:

- New constraints on the phase diagram of iron with 9 weight percent silicon between 1 bar and 16 GPa are established
- Thermal equations of state of body-centered-cubic and hexagonal-closed-packed Fe-9wt.%Si are established up to 60 GPa and 900 K
- The calculated core densities of the Moon and Mercury are consistent with previous estimates

Supporting Information:

Supporting Information may be found in the online version of this article.

Correspondence to:

B. Chen and J. Li,
binchen@hawaii.edu;
jackieli@umich.edu

Citation:

Berrada, M., Chen, B., Chao, K.-H., Peckenpaugh, J., Wang, S., Zhang, D., et al. (2024). Phase transitions and thermal equation of state of Fe-9wt.%Si applied to the Moon and Mercury. *Journal of Geophysical Research: Planets*, *129*, e2024JE008466. https://doi.org/10.1029/2024JE008466

Received 30 APR 2024
Accepted 6 OCT 2024

Author Contributions:

Conceptualization: Bin Chen, Jie Li
Funding acquisition: Bin Chen, Jie Li
Investigation: Bin Chen, Keng-Hsien Chao, Juliana Peckenpaugh, Siheng Wang, Dongzhou Zhang, Phuong Nguyen
Methodology: Bin Chen, Jie Li
Resources: Bin Chen, Dongzhou Zhang, Phuong Nguyen, Jie Li
Supervision: Bin Chen, Dongzhou Zhang, Phuong Nguyen, Jie Li
Writing – review & editing: Bin Chen, Jie Li

Phase Transitions and Thermal Equation of State of Fe-9wt.%Si Applied to the Moon and Mercury

Meryem Berrada[1,2], Bin Chen[1], Keng-Hsien Chao[1], Juliana Peckenpaugh[1], Siheng Wang[1], Dongzhou Zhang[1,3], Phuong Nguyen[1,3], and Jie Li[2]

[1]Hawaii Institute of Geophysics and Planetology, University of Hawaii at Manoa, Honolulu, HI, USA, [2]Earth and Environmental Sciences, University of Michigan, Ann Arbor, MI, USA, [3]Center for Advanced Radiation Sources, The University of Chicago, Chicago, IL, USA

Abstract Accurate knowledge of the phase transitions and thermoelastic properties of candidate iron alloys, such as Fe-Si alloys, is essential for understanding the nature and dynamics of planetary cores. The phase diagrams of some Fe-Si alloys between 1 atm and 16 GPa have been back-extrapolated from higher pressures, but the resulting phase diagram of $Fe_{83.6}Si_{16.4}$ (9 wt.% Si) is inconsistent with temperature-induced changes in its electrical resistivity between 6 and 8 GPa. This study reports in situ synchrotron X-ray diffraction (XRD) measurements on pre-melted and powder $Fe_{83.6}Si_{16.4}$ samples from ambient conditions to 60 GPa and 900 K using an externally heated diamond-anvil cell. Upon compression at 300 K, the *bcc* phase persisted up to ~38 GPa. The *hcp* phase appears near 8 GPa in the pre-melted sample, and near 17 GPa in the powder sample. The appearance of the *hcp* phase in the pre-melted sample reconciles the reported changes in electrical resistivity of a similar sample, thus resolving the low-pressure region of the phase diagram. The resulting high-temperature Birch-Murnaghan equation of state (EoS) and thermal EoS based on the Mie-Gruneisen-Debye model of the *bcc* and *hcp* structures are consistent with, and complement the literature data at higher pressures. The calculated densities based on the thermal EoS of Fe-9wt.%Si indicate that both *bcc* and *hcp* phases agree with the reported core density estimates for the Moon and Mercury.

Plain Language Summary The compositions of the interiors of planetary bodies such as the Moon and Mercury can be inferred by examining how core analogue materials (e.g., Fe-Si alloys) behave at high pressures and temperatures. However, phase transitions of Fe-Si alloys under conditions relevant to the Moon and Mercury have only been inferred from the extrapolations of data acquired at higher pressures. Additionally, electrical resistivity measurements have suggested that Fe-Si alloy containing 9 wt.% Si undergoes pressure-induced changes that are not well understood. To clarify these ambiguities, we acquired XRD patterns of Fe-9wt.%Si up to 60 GPa and 900 K using an externally heated diamond-anvil cell. The results show that Fe-9wt.% Si can exist in two different crystal structures, body-centered cubic and hexagonal close-packed, depending on the pressure-temperature conditions. The transition between these structures occurs at different pressures for the pre-melted and powder samples. By modeling how the volume of the sample changes with pressure and temperature, we found that the densities of the Moon's and Mercury's cores align closely with existing models, implying a substantial presence of Fe-9wt.%Si.

1. Introduction

Terrestrial-type bodies, such as Mercury and the Moon, exhibit a core, mantle, and crust structure similar to that of Earth. A combination of geophysical and geodetic constraints recently provided strong evidence for the presence of a lunar inner core (Briaud et al., 2023). This inner core is small, occupying approximately 15% of the Moon's radius. Remote sensing data from Apollo and subsequent missions, combined with geochemistry, sound velocity, and geodetic data, suggest that the core contains metals consisting primarily of Fe with traces of Ni and perhaps smaller amounts of S, Si, and C (Edmund et al., 2022; Kuskov & Kronrod, 2001; Sakairi et al., 2017; Terasaki et al., 2019; Weber et al., 2011; Wieczorek et al., 2006). In contrast, recent geodetic evidence suggests that Mercury's inner core occupies 30%–70% of a 1,967 ± 23 km outer core, corresponding to 20%–56% of the planet's radius (Genova et al., 2019). Understanding of the core's light element content largely comes from chemical abundances of the solar system, models based on Earth and the Moon, and data from NASA's MESSENGER spacecraft. However, the exact composition and properties of Mercury's inner core remain subjects of debate. Early studies estimate a core that is primarily metal (Fe, Ni, Co) at 99 wt.% and FeS at 1 wt.% (Morgan &

Anders, 1980). Some recent studies suggest the presence of Si, with minor S and C, considering Mercury's highly reduced conditions (Nittler et al., 2017). Combined models of elasticity and geodetic data suggest a composition with 10.5 wt.%Si (Steinbrügge et al., 2021; Terasaki et al., 2019). Identifying the core's light elements is crucial for understanding the bulk chemistry of terrestrial-type bodies, core formation processes, and its thermal evolution. As such, the Fe-Si alloy phase diagram and equation of state (EoS) are crucial for understanding the composition and internal dynamics of the cores of Mercury and the Moon.

The phase diagram of Fe-9wt.%Si holds particular interest as it approaches the expected composition of the inner cores of the Moon and Mercury. At 1 atm, Fe-9wt.%Si undergoes transitions from $D0_3$ to *B2* phase, then *B2* to *A2* phase, followed by melting (Hansen et al., 1958). The $D0_3$, *B2*, and *A2* phases represent distinct variants of the body-centered cubic (*bcc*) crystal structure that can form in Fe-Si alloys under specific conditions. In the ordered $D0_3$ phase (*Fm3m*), atoms pair with their next neighbors; in the partially ordered *B2* phase (*Pm3m*), atoms pair with their nearest neighbors; and in the disordered *A2* phase (*Im3m*), Fe and Si atoms are randomly distributed. The transition from $D0_3$ to *B2* may entail a decrease in long-range order and an increase in atomic disorder, as observed at 300 K up to 29 GPa (Fischer et al., 2013). On the other hand, the $D0_3$ phase is not observed in several studies at 300 K and high pressures (*P*), possibly due to the relatively low intensity of the $D0_3$ X-ray diffraction (XRD) peaks compared to the *B2* XRD peaks (Fischer et al., 2012; Hirao et al., 2004; Lin et al., 2003; Zhang & Guyot, 1999). In addition to the challenges in detecting the $D0_3$ signature at ambient conditions, a rapid cooling rate is found to suppress the transition from the disordered *A2* phase at high temperatures (*T*) to the partially ordered *B2* and ordered $D0_3$ phases at lower *T* (Ouyang et al., 2019; Wang et al., 2021). Each variant of the *bcc* phase exhibits different lattice constants, interatomic distances, and structural parameters that affect the physical properties of the alloys (Cui & Jung, 2017). In addition, the presence of different phases can result in changes in the mechanical and magnetic properties of the alloys (Cui & Jung, 2017). Above 20 GPa, Fe-9wt.%Si transitions from *hcp* to a mix of *hcp* and *B2*, then a mix of *fcc* and *B2*, followed by melting (Edmund et al., 2022; Fischer et al., 2013, 2014; Yokoo et al., 2023). At 16 GPa, Lin et al. (2002) confirms the appearance of a mixed *fcc* phase, although with *bcc* rather than *B2*, along the back-extrapolated boundary defined by Fischer et al. (2013). Previous studies have provided constraints on the phase diagram at either 300 K by compression without heating (Hirao et al., 2004; Lin et al., 2003; Zhang & Guyot, 1999) or at temperatures above 1000 K using laser heating methods (Edmund et al., 2022; Fischer et al., 2012, 2013, 2014; Yokoo et al., 2023). Defining these phase transitions below 1,000 K is necessary to complete the phase diagram of Fe-9wt.%Si.

To determine the stable phases at the cores of the Moon (at conditions near 5 GPa and 1,600 K) and Mercury (ranging from 10 to 40 GPa and 1,800–2,100 K), an approach involves back-extrapolating the 1 atm, 16 GPa, and above 20 GPa phase diagrams. In addition, recent electrical resistivity (ϱ) measurements of Fe-8.5wt.%Si indicate variations below the magnetic transition between 6 and 8 GPa and 500–1,000 K, although no phase transition is reported in the literature for this composition at the observed *P-T* conditions (Berrada et al., 2021). In fact, no phase transition is observed at these *P-T* conditions in Fe, while the magnetic transition, indicating the structural change from *bcc*-Fe to *fcc*-Fe, is the nearest well-defined transition. Electrical resistivity, a measure of the resistance of a material to the flow of electric current, can be influenced by a variety of factors, including the crystal structure of the material, temperature, pressure, impurities, and electron scattering mechanisms. Changes within the *bcc* phase may be due to changes in the lattice structure, interatomic distances, and other structural parameters. In turn, such changes have the potential to impact the density of free electrons, which consequently affects the material's ϱ. The interplay of these factors emphasizes the link between structural variations and electrical properties within materials. Furthermore, changes in a material's electrical properties can influence the dynamics of fluid motion and the generation of a magnetic field, as well as impact the efficiency of heat transfer processes within terrestrial-type cores (Baym & Heiselberg, 1997).

This study presents a comprehensive investigation of the structural and density (ρ) characteristics of Fe-Si alloys up to 60 GPa, covering the internal conditions of the Moon and Mercury. The resulting EoS for Fe-9wt.%Si in the low *P-T* region of the phase diagram reduces the dependence on back-extrapolations from data obtained at higher *P*.

2. Methods

The starting material, Fe-9wt.%Si (99.5% purity, GoodFellow Inc.), was initially in powder form. A molten sample was prepared in a muffle furnace following the procedure described by Berrada et al. (2020) to replicate

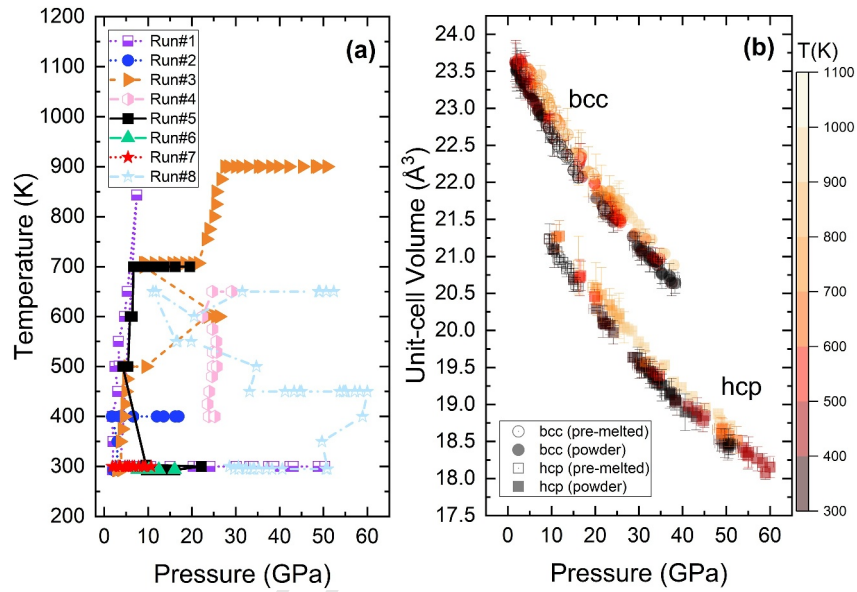

Figure 1. (a) P-T path of all experimental runs. (b) Unit-cell volume of Fe-9wt.%Si from indexed bcc and hcp phases. The notations "pre-melted" and "powder" refer to the state of the starting material.

conditions similar to those where ϱ variations were observed. This sample is hereafter referred to as the "pre-melted" sample. A second set of experiments was conducted using the starting material in powder form, hereafter referred to as the "powder" sample. In the powder sample experiments, pellets of Fe-9wt.%Si were made by crushing grains of the starting material between two moissanite anvils to a thickness of ∼10 μm. In the molten sample experiments, a flake of the alloy was carefully carved off and then flattened between two moissanite anvils to a thickness of ∼10 μm. The samples were loaded into separate BX-90 diamond anvil cells (DAC) equipped with 300 μm culet diamonds. The gaskets, made of rhenium (Re), were pre-indented to ∼30 μm and laser drilled to create a sample chamber of 150 μm in diameter. KCl served as the pressure-transmitting medium. After loading, the DACs were dried at 400 K under vacuum for a minimum of 2 hr before sealing. In situ synchrotron XRD measurements were conducted up to 50 GPa and 900 K in the Externally Heated-Diamond ANvil Cell Experimentation system (EH-DANCE) system, as described in Wang et al. (2023), at the 13-BMC beamline of the Advanced Photon Source, Argonne National Laboratory. The incident monochromatic beam had an energy of 28 KeV (λ = 0.434 Å) and was focused on a spot of 9 × 4 μm^2. Compression and decompression membranes around the DAC provided precise *P* control. High *T*'s were generated by applying DC voltage to a microheater with tungsten wires wound around a sintered pyrophyllite cylinder that is placed around the sample (Lai et al., 2020). Temperature was monitored using a Type-K thermocouple situated ∼500 μm from the culet. The water-cooled EH-DANCE enclosure maintained a nitrogen atmosphere, enabling extended exposure to high *T*. Eight runs were conducted: two with the molten sample (Runs #1, 5) and six with the sample in powder form. In all experiments, *P* was determined using the thermal EoS of Au (Fei et al., 2007). The uncertainty in *P* corresponds to the uncertainty in the volume (*V*) of Au, while that of *T* is set to 5 K based on the thermocouple's stability. X-ray diffraction patterns were processed using DIOPTAS (Prescher & Prakapenka, 2015), and the lattice parameters were refined using PDIndexer (Seto et al., 2010). The parameters for the *P-V-T* EoS of Fe-9wt.%Si were derived using PythEOS (Shim, 2017).

3. Results

3.1. Structures and Unit-Cell Volumes of Fe-9wt.%Si

Figure 1a illustrates the data encompassed within the *P-T* space, while Figure 1b portrays the trajectory of the *P-V* conditions. The measurements extend to pressures surpassing 60 GPa and temperatures reaching 900 K. Upon conducting XRD measurements on Fe-9wt.%Si, only *bcc* and *hcp* phases were observed. The characteristic diffraction signatures of the $D0_3$ and *B2* phases, which include unique additional peaks typically observed around the 2-theta angle of 6–7°, were not observed. While the powder sample is anticipated to exhibit a higher degree of

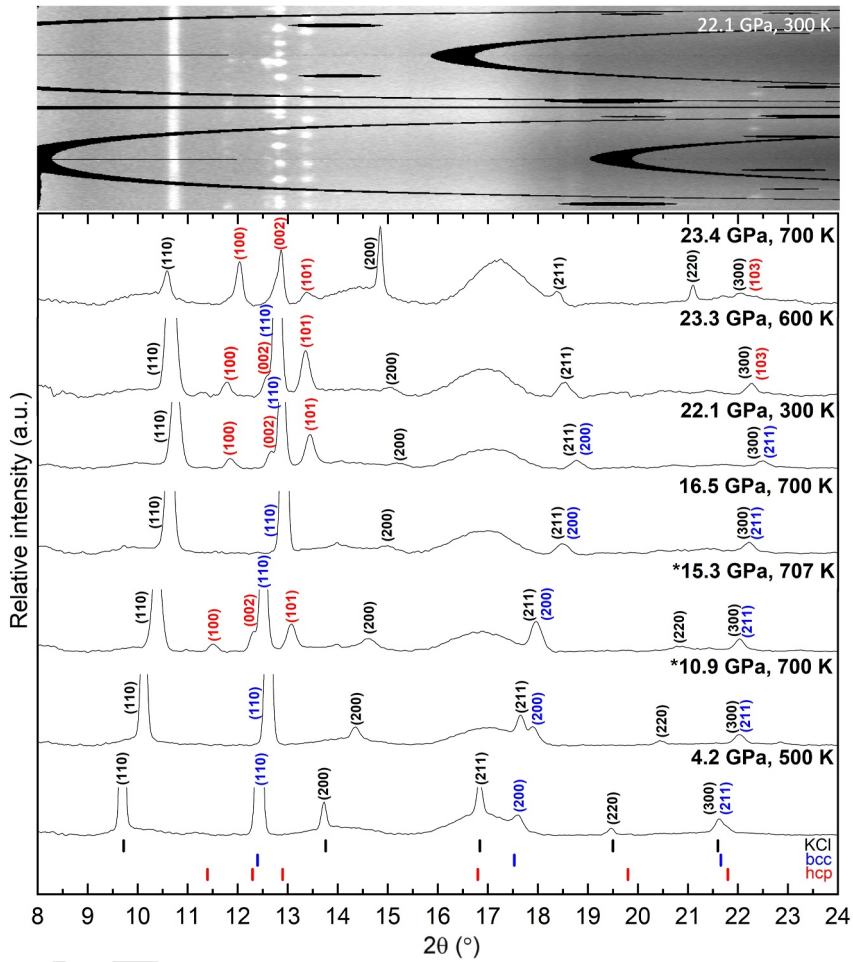

Figure 2. Selected X-ray diffraction (XRD) measurements of the Fe-9wt.%Si within KCl pressure medium. The indexed peaks for the bcc and hcp phases are labeled. The top "cake" representation of 2D XRD image shows an example of the polycrystal structure observed for both bcc and hcp Fe-9wt.%Si at 22.1 GPa and 300 K. The pressures marked with an asterisk (*) indicate the measurements conducted on the pre-melted sample, whereas the other trends pertain to the powder sample.

ordering compared to the molten counterpart due to the latter being quenched after reaching the liquid state (Berrada et al., 2020), the presence of short- and long-range orders, typically represented by the $D0_3$ and $B2$ phases respectively (Numakura et al., 1972; Ohnuma et al., 2012; Secco, 2017), is not evident throughout the P-T range studied. In addition, results show no significant discrepancy between the powder and pre-melted sample signals (Glaser & Ivanick, 1956; Numakura et al., 1972; Secco, 2017). Figure 2 shows representative XRD patterns across the investigated P-T range, and a typical polycrystalline signal from the *bcc* and *hcp* structures. At similar P-T conditions, the pre-melted sample exhibits evidence of *hcp* and *bcc* structures, while the powder sample only shows evidence of the *bcc* phase.

3.2. Thermal Equation of State of Fe-9wt.%Si

The experimental P-V-T data sets for *bcc* and *hcp* Fe-9wt.%Si were used to fit the high T third-order Birch-Murnaghan EoS (BM3) as well as to the Mie-Grüneisen-Debye (MGD) model, as illustrated in Figures 3 and 4. At 300 K, BM3 is expressed as:

$$P(V, 300\ K) = \frac{3}{2}K_0\left[\left(\frac{V_0}{V}\right)^{\frac{7}{3}} - \left(\frac{V_0}{V}\right)^{\frac{5}{3}}\right]\left[1 + \frac{3}{4}\left(K_0' - 4\right)\left(\left(\frac{V_0}{V}\right)^{\frac{2}{3}} - 1\right)\right] \quad (1)$$

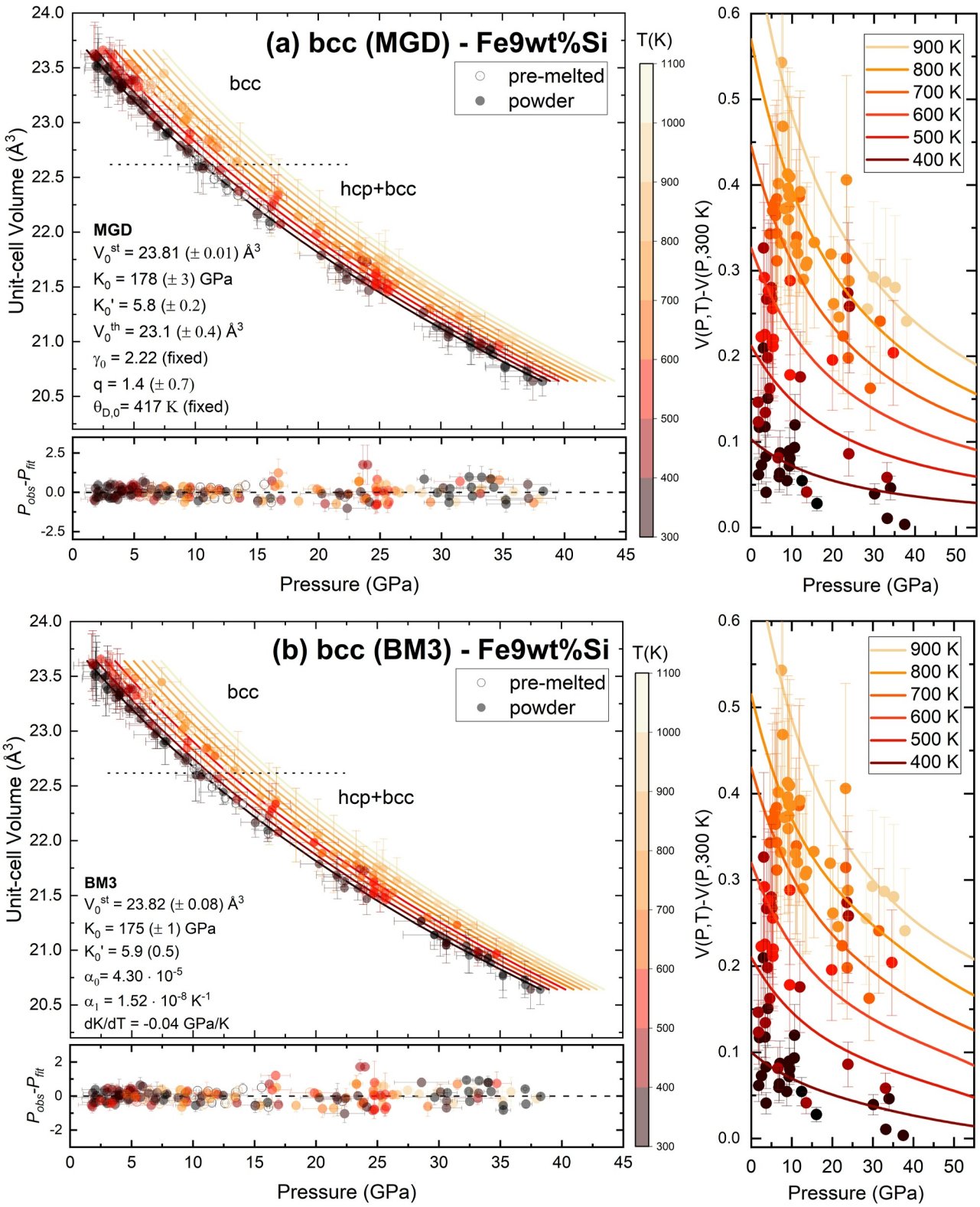

Figure 3. (a) MGD and (b) BM3 fits of the bcc - Fe-9wt.%Si. Fit parameters are illustrated in the respective figures. The right subplots show the high temperature volume difference from that at 300 K at corresponding pressures. The "st" and "th" superscript refer to the static and thermal parameters, respectively. The notations "pre-melted" and "powder" refer to the state of the starting material. The bottom subplots show the difference between the observed pressures and those obtained from the fits.

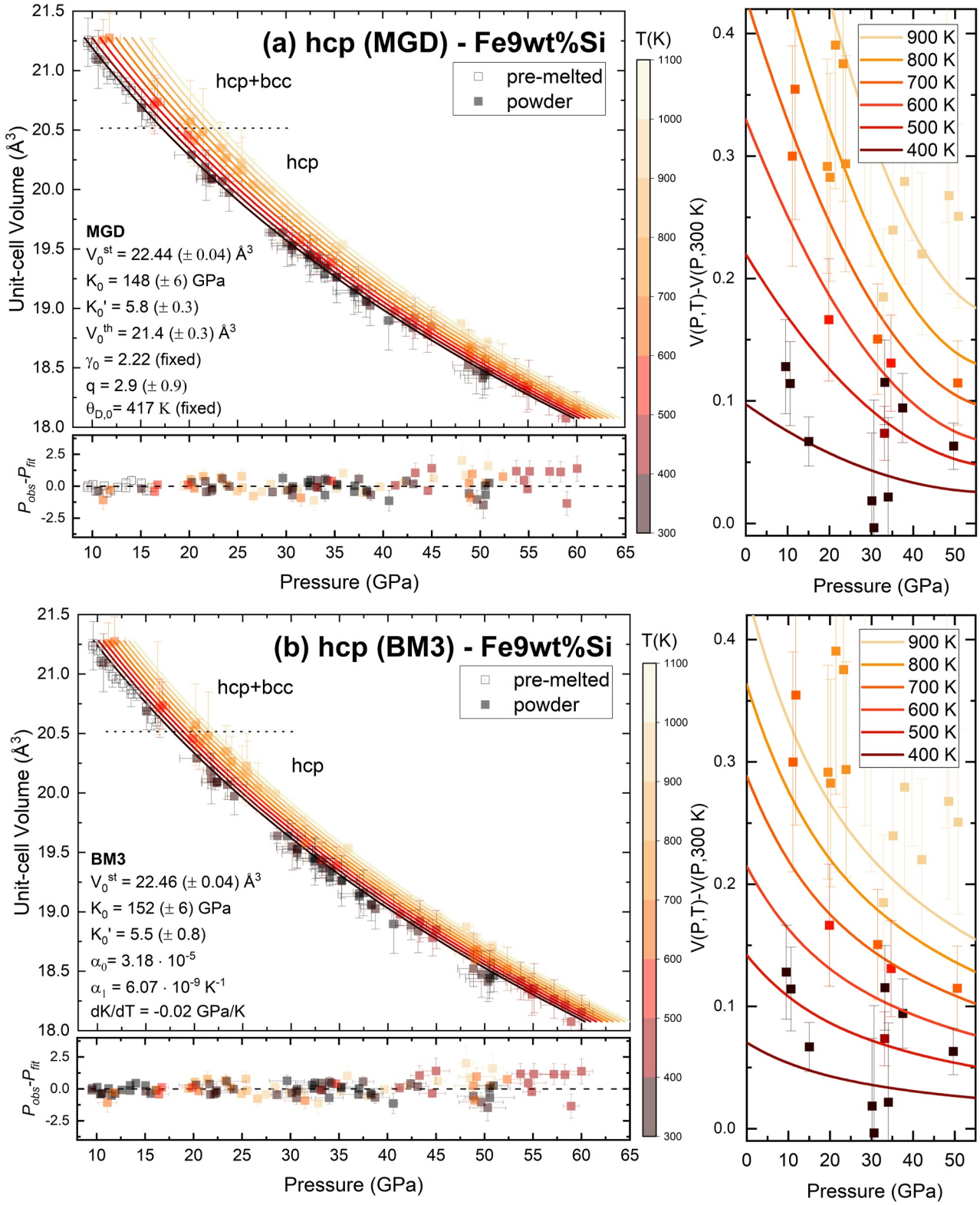

Figure 4. (a) MGD and (b) BM3 fits of the hcp - Fe-9wt.%Si. Fit parameters are illustrated in the respective figures. The right subplots show the high temperature volume difference from that at 300 K at corresponding pressures. The "st" and "th" superscript refer to the static and thermal parameters, respectively. The notations "pre-melted" and "powder" refer to the state of the starting material. The bottom subplots show the difference between the observed pressures and those obtained from the fits.

where K_0 is the isothermal bulk modulus at 1 bar, K_0' is the pressure derivative of the bulk modulus, V is volume, and V_0 is the zero-pressure volume (Birch, 1952). At high T, BM3 has T dependent volume and bulk modulus such that the following expressions are satisfied:

$$V(T) = V_0\left[1 + \alpha_0(T - 300) + \frac{1}{2}\alpha_1(T - 300\ K)^2\right] \tag{2}$$

$$K(T) = K_0 + \frac{dK}{dT}(T - 300\ K) \tag{3}$$

where a_0 and a_1 are constants. On the other hand, the MGD model assumes separate terms for P at 300 K and P at high T, such that

$$P(V, T) = P(V, 300\ K) + \Delta P_{th}(V, T) \tag{4}$$

where $\Delta P_{th}(V, T)$ is expressed as

$$\Delta P_{th}(V, T) = \frac{\gamma\ (V)}{V}[E_{th}(V, T) - E_{300\ K}(V, 300\ K)] \tag{5}$$

where E_{th} describes the Debye model of vibrational energy, and γ_0 is the Grüneisen parameter, such that

$$E_{th}(V, T) = 9nR\ T\left(\frac{T}{\theta_D}\right)^3 \int_0^{\frac{\theta_D}{T}} \left(\frac{x^3}{\exp(x) - 1}\right) dx \tag{6}$$

using n as the number of atoms per unit formula, R as the gas constant, the Debye temperature $\theta_{D,0}$ with $\theta_D = \theta_{D,0} \exp\left[\frac{\gamma_0 - \gamma(V)}{q}\right]$, and $\gamma\ (V) = \gamma_0\left(\frac{V}{V_0}\right)^q$ with constant q. Only γ_0 and $\theta_{D,0}$ were fixed during fitting the MGD EoS, following the values of pure Fe, as typically done in Fe-Si modeling (Fischer et al., 2014). The fit results are listed in Figures 3 and 4 and Table S1 in Supporting Information S1. The smaller volume associated with the *hcp* phase is a reflection of the inherently more compact and closely packed crystal lattice of the *hcp* phase as expected (Fischer et al., 2014).

When considering the difference in V between high-T and 300 K (right panels of Figures 3 and 4), both models show comparable accuracy in fitting the high-T *bcc* data, while the MGD model provides a better fit of the high-T *hcp* data at 900 K than the BM3 model, despite similar pressure residuals. The data quality appears to be consistent between the *bcc* and *hcp* phases despite the greater availability of data for the *bcc* phase at 300 K. The better constraint of the ambient fit in the *bcc* phase suggests that the high-T modeling will inherently be more accurate in the *bcc* phase than in the *hcp* phase. Additionally, the BM3 model features 6 free parameters, whereas the MGD model has 5 free parameters and 2 fixed parameters. Having fewer free parameters can lead to a more robust and stable fitting process, and the presence of fixed parameters can help constrain the model and prevent overfitting. These factors could allow the MGD model to more accurately capture the nuances at high-T in the *hcp* phase.

3.3. *P-T* Phase Diagram of Fe-9wt.%Si

Results from XRD measurements are compiled in Figure 5 and compared with reported T-dependent changes in ϱ measurements ($d\varrho/dT$). Electrical resistivity measurements of Fe-8.5wt.%Si indicate fluctuations at the melting boundary as well as at and below the magnetic transition. The magnetic transition in a material is typically associated with a change in the magnetic ordering and alignment of the magnetic moments of the atoms. This transition can lead to a sudden change in ϱ of the material because the magnetic ordering affects the scattering of electrons. On the other hand, structural transitions, such as the *bcc* to *hcp* + *bcc* transition, may be identified by smooth fluctuations in ϱ. The change in ϱ during structural transitions is generally more gradual because it is primarily influenced by the lattice scattering of electrons as the crystal lattice is rearranged rather than the

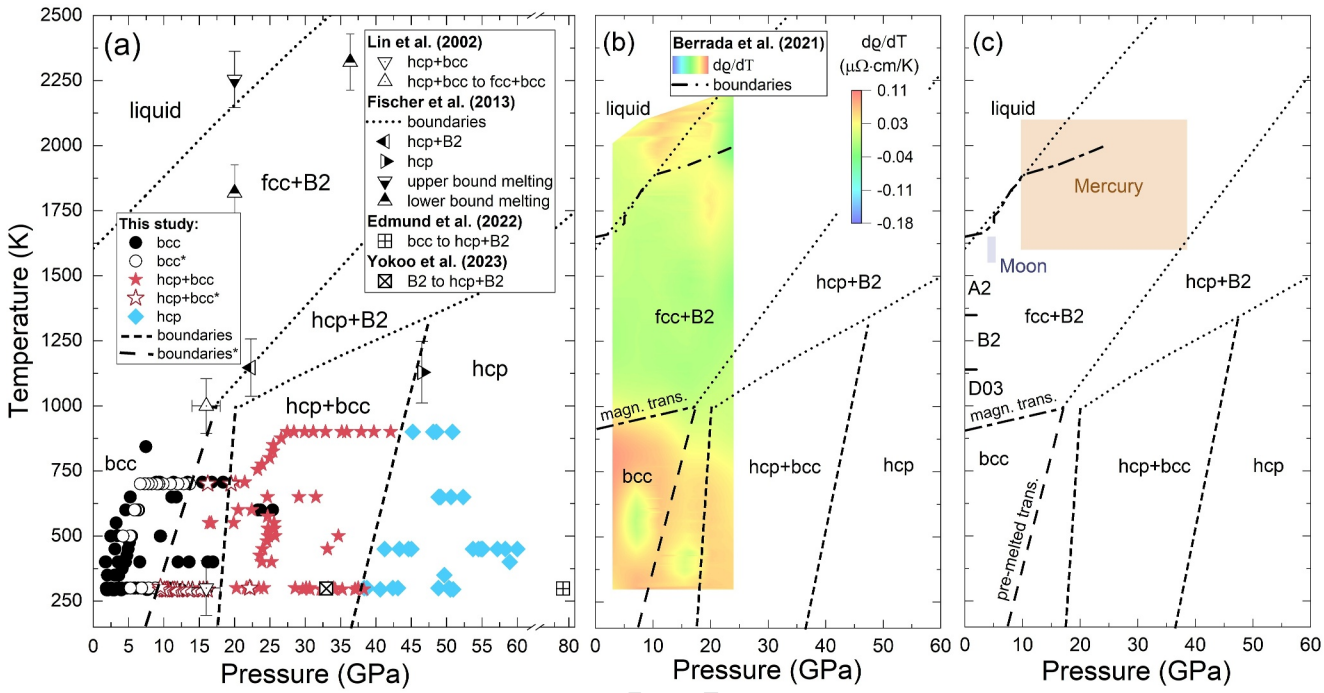

Figure 5. (a) Phase diagram of Fe-9wt.%Si up to 60 GPa including available literature (Edmund et al., 2022; Fischer et al., 2013; Lin et al., 2002; Yokoo et al., 2023). Note that Yokoo et al. (2023) reported the transition for Fe-7wt.%Si. The * denotes measurements done on the pre-melted sample. The thick black dashed line represents the estimated phase boundary of the pre-melted sample, while the thick black dotted lines represent those of the powder sample. (b) Changes in electrical resistivity (d ϱ/dT) of Fe-8.5wt.%Si (Berrada et al., 2021) are reported via the contour map. (c) Resulting phase boundaries with the pressure range for the cores of the Moon and Mercury. The $D0_3$, *B2* and *A2* phases at ambient pressure are also illustrated (Hansen et al., 1958).

magnetic interactions. The fluctuations in ϱ indicate a pattern of low-high-low $d\varrho/dT$ regions below 20 GPa. In this region, the XRD measurements indicate a transition from *bcc* to *hcp* + *bcc* in the pre-melted sample, which seems to occur before that observed in the powder sample. The behavior of the pre-melted sample may be comparable to that of amorphous materials, which can undergo phase transitions more readily than crystalline materials of the same composition, as they require less energy to transition to a more stable crystalline state (Çelikbilek et al., 2012). Achieving equilibrium for phase stability relations can be challenging, which may explain the observed metastable survival of the starting phase. Similarly, the pressure interval where both *bcc* and *hcp* are observed is likely broader than the equilibrium pressure interval of the *bcc* to *hcp* transition. The *bcc* to *hcp* + *bcc* phase boundary observed in the pre-melted sample in this study aligns with the region of high $d\varrho/dT$ from measurements on a similar pre-melted sample (Berrada et al., 2021). However, both transitions are in agreement with reported structures by Lin et al. (2002) but occur at *P* much lower than reported by Edmund et al. (2022) or Yokoo et al. (2023) for Fe-7wt.%Si. At higher *P*, a transition into pure *hcp* phase is observed in the powder sample that is in agreement with structures reported by Fischer et al. (2013). It is challenging to determine whether the transition pressure from *hcp* + *bcc* to pure *hcp* is consistent between the pre-melted and powder samples, as the pre-melted sample remained a mixture of *hcp* + *bcc* at the highest experimental pressure of 20 GPa. Below 10 GPa, the estimated melting boundary, as reported by Fischer et al. (2013), aligns with the high-low-high $d\varrho/dT$ fluctuations at high temperatures (Berrada et al., 2021). Above 10 GPa, while the lower and upper bounds of the estimated melting boundary agree with the $d\varrho/dT$ fluctuations, the boundary itself is at higher temperatures. This discrepancy may be attributed to the behavior of the pre-melted sample from Berrada et al. (2021), which appears to undergo phase transitions earlier than the powder sample from Fischer et al. (2013). No additional changes in ϱ are observed within the low temperature region. Thus, any potential change in order (i.e., changes between $D0_3$, *B2*, *A2*) missed during XRD measurements do not seem to influence ϱ, and should therefore have negligible effect on the intensity and duration of a dynamo in planetary cores (Hamid et al., 2023). A summary of the phase transitions of Fe-9wt.%Si up to 60 GPa is illustrated in Figure 5b along with the pressure range at the cores of the Moon and Mercury.

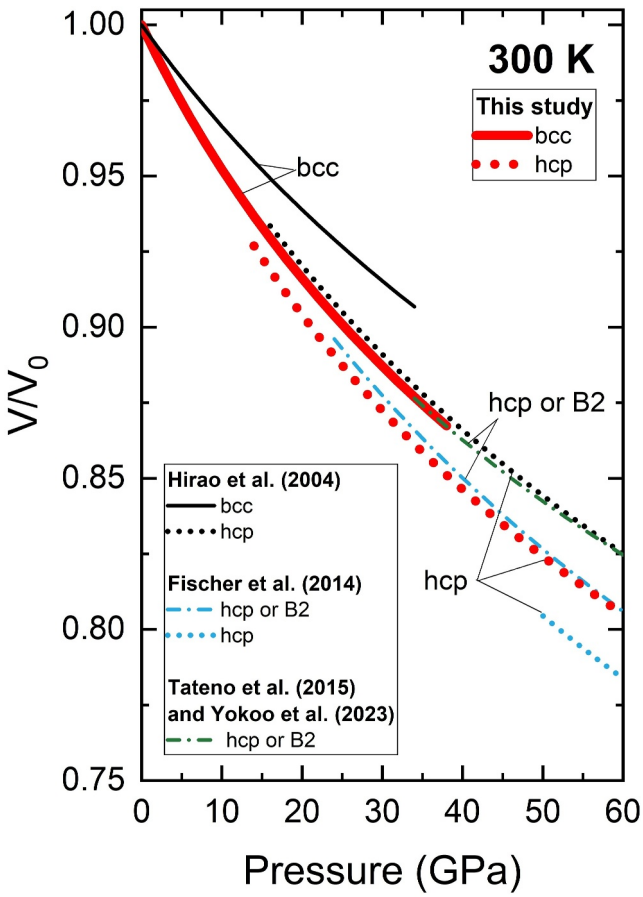

Figure 6. Volume ratio of the unit cell of Fe-9wt.%Si at 300 K compared with the literature (Fischer et al., 2014; Hirao et al., 2004; Tateno et al., 2015; Yokoo et al., 2023). The $D0_3$ trend by Fischer et al. (2014) overlaps the bcc trend from this study within the measured range of 1 bar–29 GPa. The hcp trend by Tateno et al. (2015) overlaps the *B2* trend by Yokoo et al. (2023). The EoS parameters from this study and the literature are summarized Table S1 in Supporting Information S1.

4. Discussion and Implications

This study presents a multi-technique approach that combines XRD measurements and literature ϱ results to identify crucial phase transitions in Fe-alloys. Polycrystalline *bcc* and *hcp* phases of Fe-9wt.%Si were observed up to 60 GPa and 900 K in both pre-melted and powder samples. The pre-melted sample has expressed a *bcc* to *hcp* + *bcc* phase transition at pressures lower than those observed in the powder sample, possibly due to its predisposition to transition to a stable state. This phase transition from *bcc* to *hcp* + *bcc* aligns with the discernible variations in ϱ as previously noted for the pre-melted Fe-Si alloy (Berrada et al., 2021). These observed ϱ variations can be attributed to shifts in electron scattering mechanisms which seem to be related to these structural changes. These correlations complete the phase diagram between 1 bar and 16 GPa while contributing to our understanding of the intricate interplay between crystallographic, chemical, and electronic transformations in this complex system. Phase transitions that are accompanied by noticeable ϱ changes, such as the *bcc* to *hcp* transition, are likely to influence the duration and intensity of a core dynamo in terrestrial-type cores (Hamid et al., 2023).

The resulting parameters V/V_0 from the 300 K BM3 EoS fit of the *bcc* and *hcp* phases are compared to the literature in Figure 6. The results align with the $D0_3$ trend as documented by Fischer et al. (2014) and the *B2* trend by Yokoo et al. (2023). In contrast, Hirao et al. (2004) deliberated on the likelihood of non-hydrostatic conditions influencing an overestimation of K_0 for Fe-8.7wt.%Si, offering a plausible explanation for the elevated trajectory of their V/V_0. The *hcp* trend from this study diverges from the trends identified by Hirao et al. (2004), Fischer et al. (2014), and Tateno et al. (2015) although it is in agreement with the mixed phase trend of *hcp* or *B2* (Fischer et al., 2014). The discrepancies in the reported EoS could be associated with the challenges in distinguishing the signature peaks of the *hcp* and *bcc* phases, as chemical diffusion causes the diffraction patterns of two phases to intermingle. They could also partly stem from the varying hydrostatic environments in different experimental configurations. Additionally, Fischer et al. (2014) fitted their EoS for *hcp* or *B2,* and *hcp* phases solely for high-*T* data, whereas the other EoS's were based on measurements at 300 K. Nonetheless, in this study, no obvious change in the *V* of *hcp* phase is observed once the *bcc* phase disappeared, which stands in contrast to the observations made by Fischer et al. (2014) near 50 GPa. Further investigation into the stability and behavior of these phases under extreme conditions is necessary to clarify these discrepancies.

Stable solid phases provide fundamental constraints on the planet's ρ profile, heat distribution, and the underlying core crystallization regime. In fact, thermal EoS is required to estimate the ρ of Fe-Si alloys at relevant *P-T* conditions, allowing insightful comparisons with seismological models. Results from this study are used to calculate the core ρ of the Moon and Mercury, see Table 1. In general, the core ρ of these terrestrial-type bodies is anticipated to surpass the values reported within this study, stemming from the anticipation of the *fcc* phase coexisting alongside the *bcc* phase at the projected core *T* of both the Moon and Mercury. On the other hand, the incorporation of additional light elements is expected to reduce the core ρ. Similarly, a larger inner core radius, for both the Moon (Matsuyama et al., 2016; Weber et al., 2011; Williams et al., 2014) and Mercury (Harder & Schubert, 2001; Van Hoolst & Jacobs, 2003), translates to lower average *P* and *T*, accompanied by a slightly lower ρ, albeit still within uncertainties.

At the lunar core conditions, the calculated ρ from the BM3 and MGD models exhibit variations spanning several standard deviations. Considering that the high-*T bcc* data are fit similarly with both models, the ρ is estimated to range from 5.57 to 5.94 ± 0.01 g/cm^3 for a bcc Fe-Si rich lunar core at the inner-core boundary (ICB). On the other hand, the high-*T hcp* data is best fit with the MGD model, which suggest a ρ (6.31 ± 0.01 g/cm^3) in

Table 1
Parameters Used to Calculate the Density at the Lunar ICB and Mercury's CMB Based on the EoS Results for bcc and hcp Fe-9wt.%Si

	Core radius (km)	T (K)	P (GPa)	Density (g/cm^3)		EoS
Moon	381 (+28/−51)[a]	–	–	7.800 [a-b]		–
	330 ± 20[b]					
	200–380[c]					
	258 ± 40[d]	–	4.3–4.6[d]	7.822 ± 1.615 (IC)[d]		–
				5.025 ± 0.604 (OC)[f]		
		1,595 ± 2 [e*]	4.96 ± 0.05 [f]	5.57 ± 0.01[j*]		BM3 (*bcc*)
				5.94 ± 0.01[j*]		MGD (*bcc*)
				6.44 ± 0.01[j*]		BM3 (*hcp*)
				6.31 ± 0.01[j*]		MGD (*hcp*)
Mercury	1,860 ± 80[g]	1,400 K[g]	10[g]	8.160 (*fcc*-Fe, IC)[g]		–
				5.808 (*fcc*-FeS, OC)[g]		
	2,000 ± 420[h*]	1,700 K[h*]	–	7.225 ± 0.075[h*]		–
	2020 ± 30[i]	1,600–2,100[i]	10–40[g]	6.980 ± 0.28[i]		–
				5.8 ± 0.1[j*]	6.7 ± 0.1[j*]	BM3 (*bcc*)
				6.1 ± 0.1[j*]	6.7 ± 0.1[j*]	MGD (*bcc*)
				6.6 ± 0.1[j*]	7.6 ± 0.1[j*]	BM3 (*hcp*)
				6.5 ± 0.1[j*]	7.3 ± 0.1[j*]	MGD (*hcp*)

[a]Matsuyama et al. (2016). [b]Weber et al. (2011). [c]Williams et al. (2014). [d]Briaud et al. (2023). [e*]Laneuville et al. (2014). [f]Garcia et al. (2012). [g]Van Hoolst and Jacobs (2003). [h*]Harder and Schubert (2001). [i]Hauck et al. (2013). [j*]This study. The density at Mercury's core is calculated at 10 GPa (left column) and 40 GPa (right column). The * indicates experimental studies, while the other studies are based on geophysical observations.

agreement within uncertainty with recently reported values from geophysical and geodetic constraints (Briaud et al., 2023). Assuming a liquid Fe-8.7wt.%Si rich outer core (Nakajima et al., 2020), the ρ jump at the ICB would be at least 7% with a *bcc* inner core, see Figure 7. Since the EoS of *fcc* Fe-9wt.%Si is unavailable, the ρ jump at the ICB would be at most 38% if a pure *fcc* Fe inner core is considered. On the other hand, the trends from Fischer et al. (2014) suggest a ρ decrease at the ICB, potentially indicating a complex interplay between phase transitions and core dynamics.

At Mercury's outer core conditions, the ρ for *bcc* and *hcp* phases calculated using both EoS models are internally consistent within one to two standard deviations. Any potential discrepancy between the models would be obscured by the significant range of T encountered in Mercury's outer core environment. An agreement is found between this study and the reported *fcc*-FeS rich outer core model from Van Hoolst and Jacobs (2003), along with the *fcc*-Fe rich outer core model from Harder and Schubert (2001). The *bcc* and *hcp* ρ from this study agree within uncertainty with the estimated mean ρ at the core-mantle boundary (CMB) by Hauck et al. (2013). The general lower results from this study may partially be due to the expected higher ρ of the *fcc* phase not accounted for in this study. In this case, assuming a liquid Fe-8.7wt.%Si rich outer core (Nakajima et al., 2020), the ρ jump at the ICB would be at least 7% and at most 33% if a pure *fcc* Fe inner core is considered.

The MGD EoS of Fe-9wt.%Si in *hcp or B2* structure derived by Fischer et al. (2014) from higher T measurements corresponds to ρ of ~5.1 g/cm^3 at the lunar ICB condition and ~5.2–5.9 g/cm^3 at Mercury's CMB condition. Their mixed phase aligns with the *hcp* phase observed here (Figure 6), but the *hcp* densities in this study from the MGD model are considerably higher for both the Moon (6.31 ± 0.01 g/cm^3) and Mercury (6.5–7.3 ± 0.01 g/cm^3). The discrepancies are likely associated with extrapolating measurements at 900 K to 1,400–2,100 K in this study, back-extrapolating measurements at high-T to 300 K in Fischer et al. (2014), and the differences in ambient condition data between the two studies.

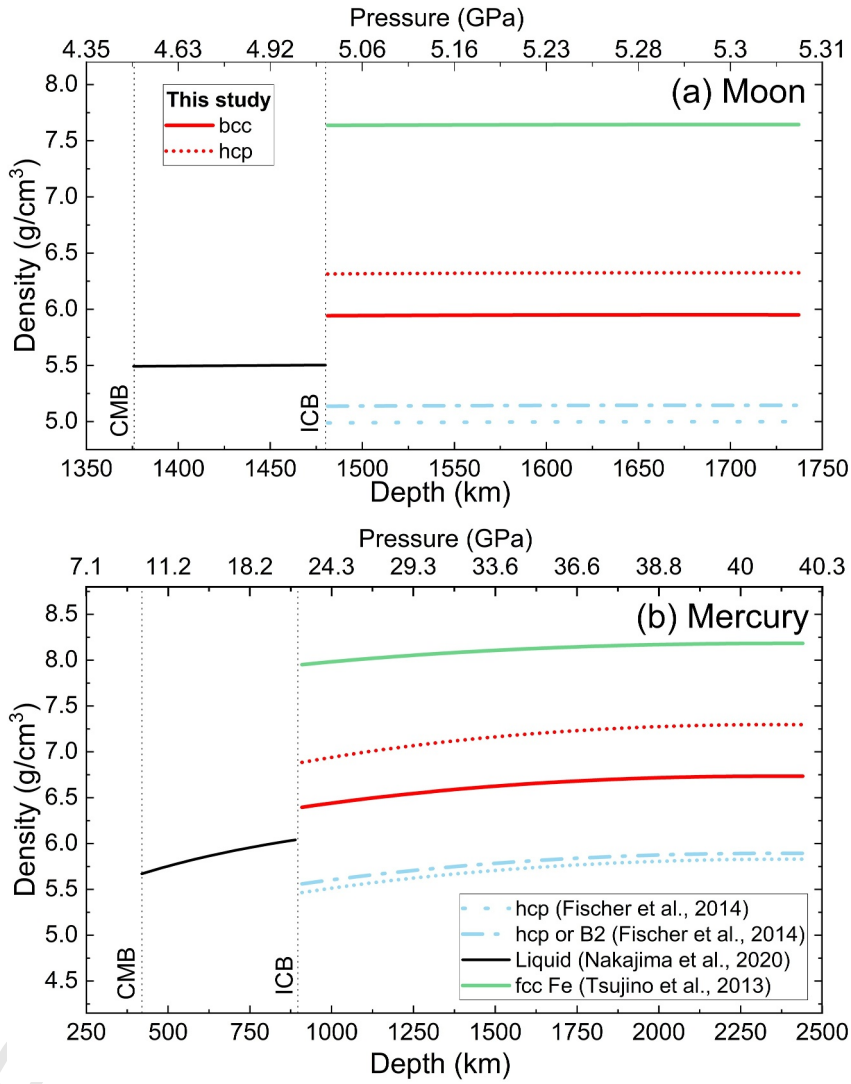

Figure 7. Density profiles of the Fe-9wt.%Si rich cores of the (a) Moon and (b) Mercury compared to other experimental studies (Fischer et al., 2014; Nakajima et al., 2020; Tsujino et al., 2013). The bcc and hcp profiles from this study are based on the MGD models. Liquid Fe-8.7wt.%Si (Nakajima et al., 2020) is used to represent the outer core composition, from the core-mantle boundary (CMB) to inner-core boundary (ICB). The density of fcc Fe is displayed as a reference for the upper-bound density of fcc Fe-9wt.%Si, as it is not available in the literature. The density profiles are based on the pressure-depth and temperature-depth profiles by Laneuville et al. (2014) and Buske (2006) respectively for the Moon, and from Garcia et al. (2012) and van Hoolst et al. (2007) respectively for Mercury.

In conclusion, this study finds that a solid core predominantly composed of *bcc* and/or *hcp* Fe-9wt.%Si would exhibit a density consistent with estimates derived from geophysical and geodetic constraints for both the Moon and Mercury, as shown in Table 1. However, the anticipated *fcc* phase in the cores of these terrestrial-type bodies could lead to a density increase at the ICB that aligns more closely with the geodetic constraints, potentially providing a more accurate picture of these bodies' internal structures and evolutionary histories. Further research is necessary to explore the role of additional light elements and complex phase transitions under extreme conditions as well as their implications for the thermal and magnetic evolution of planetary cores.

Conflict of Interest

The authors declare no conflicts of interest relevant to this study.

Data Availability Statement

All experimental data are available in Berrada (2024).

Acknowledgments
This work was supported by funds to M.B. from the Natural Sciences and Engineering Research Council of Canada (PDF – 567732 – 2022) and the Fonds de Recherche Nature et Technologies du Quebec (B3X 317379), National Science Foundation (NSF) Grants (EAR-1829273) and NASA Grants (80NSSC22K0138, 80NSSC21K0597) to B.C., and NSF Grant (EAR-2317024) to J.L. D. Z. acknowledges the support from NSF Grant EAR-2246686. Portions of this work were performed at GeoSoilEnviroCARS (The University of Chicago, Sector 13), Advanced Photon Source, Argonne National Laboratory. GeoSoilEnviroCARS is supported by the National Science Foundation-Earth Sciences (EAR-1634415). This research used resources of the Advanced Photon Source, a U.S. Department of Energy (DOE) Office of Science User Facility operated for the DOE Office of Science by Argonne National Laboratory under Contract No. DE-AC02-06CH11357. The manuscript was improved by comments from the Editorial team and reviewers.

References

Baym, G., & Heiselberg, H. (1997). The electrical conductivity in the early universe. *Physical Review Journal*, *D56*, 5254–5259. https://doi.org/10.1103/PhysRevD.56.5254

Berrada, M. (2024). Data - Phase transitions and thermal equation of state of Fe9Si [Dataset]. *Mendeley Data, V2*. https://doi.org/10.17632/VXD746SMCP.4

Berrada, M., Secco, R. A., & Yong, W. (2021). Adiabatic heat flow in Mercury's core from electrical resistivity measurements of liquid Fe-8.5 wt%Si to 24 GPa. *Earth and Planetary Science Letters*, *568*, 117053. https://doi.org/10.1016/j.epsl.2021.117053

Berrada, M., Secco, R. A., Yong, W., & Littleton, J. A. H. (2020). Electrical resistivity measurements of Fe-Si with implications for the early lunar dynamo. *Journal of Geophysical Research: Planets*, *125*(7), e2020JE006380. https://doi.org/10.1029/2020JE006380

Birch, F. (1952). Elasticity and constitution of the Earth's interior. *Journal of Geophysical Research (1896-1977)*, *57*(2), 227–286. https://doi.org/10.1029/JZ057i002p00227

Briaud, A., Ganino, C., Fienga, A., Mémin, A., & Rambaux, N. (2023). The lunar solid inner core and the mantle overturn. *Nature*, *617*(7962), 743–746. https://doi.org/10.1038/s41586-023-05935-7

Buske, M. (2006). *Three-dimensional thermal evolution models for the interior of Mars and Mercury*. University of Göttingen.

Çelikbilek, M., Ersundu, A. E., & Aydın, S. (2012). Crystallization kinetics of amorphous materials. *Advances in Crystallization Processes*, 127–162. https://doi.org/10.5772/2672

Cui, S., & Jung, I.-H. (2017). Critical reassessment of the Fe-Si system. *Calphad*, *56*, 108–125. https://doi.org/10.1016/j.calphad.2016.11.003

Edmund, E., Morard, G., Baron, M. A., Rivoldini, A., Yokoo, S., Boccato, S., et al. (2022). The Fe-FeSi phase diagram at Mercury's core conditions. *Nature Communications*, *13*(1), 387. https://doi.org/10.1038/s41467-022-27991-9

Fei, Y., Ricolleau, A., Frank, M., Mibe, K., Shen, G., & Prakapenka, V. (2007). Toward an internally consistent pressure scale. *Proceedings of the National Academy of Sciences*, *104*(22), 9182–9186. https://doi.org/10.1073/pnas.0609013104

Fischer, R. A., Campbell, A. J., Caracas, R., Reaman, D. M., Dera, P., & Prakapenka, V. B. (2012). Equation of state and phase diagram of Fe–16Si alloy as a candidate component of Earth's core. *Earth and Planetary Science Letters*, *357–358*, 268–276. https://doi.org/10.1016/j.epsl.2012.09.022

Fischer, R. A., Campbell, A. J., Caracas, R., Reaman, D. M., Heinz, D. L., Dera, P., & Prakapenka, V. B. (2014). Equations of state in the Fe-FeSi system at high pressures and temperatures. *Journal of Geophysical Research: Solid Earth*, *119*(4), 2810–2827. https://doi.org/10.1002/2013JB010898

Fischer, R. A., Campbell, A. J., Reaman, D. M., Miller, N. A., Heinz, D. L., Dera, P., & Prakapenka, V. B. (2013). Phase relations in the Fe–FeSi system at high pressures and temperatures. *Earth and Planetary Science Letters*, *373*, 54–64. https://doi.org/10.1016/j.epsl.2013.04.035

Garcia, R. F., Gagnepain-Beyneix, J., Chevrot, S., & Lognonné, P. (2012). Erratum to "very preliminary reference Moon model", by R.F. Garcia, J. Gagnepain-Beyneix, S. Chevrot, P. Lognonné [Phys. Earth Planet. Inter. 188 (2011) 96–113]. *Physics of the Earth and Planetary Interiors*, *202–203*, 89–91. https://doi.org/10.1016/j.pepi.2012.03.009

Genova, A., Goossens, S., Mazarico, E., Lemoine, F. G., Neumann, G. A., Kuang, W., et al. (2019). Geodetic evidence that Mercury has a solid inner core. *Geophysical Research Letters*, *46*(7), 3625–3633. https://doi.org/10.1029/2018GL081135

Glaser, F. W., & Ivanick, W. (1956). Study of the Fe-Si order-disorder transformation. *Journal of Occupational Medicine*, *8*(10), 1290–1295. https://doi.org/10.1007/bf03377868

Hamid, S. S., O'Rourke, J. G., & Soderlund, K. M. (2023). A long-lived lunar magnetic field powered by convection in the core and a basal Magma ocean. *The Planetary Science Journal*, *88*(5), 4. https://doi.org/10.3847/PSJ/accb99

Hansen, M., Anderko, K., & Salzberg, H. W. (1958). Constitution of binary alloys. *Journal of the Electrochemical Society*, *105*(12), 260C–261C. https://doi.org/10.1149/1.2428700

Harder, H., & Schubert, G. (2001). Sulfur in Mercury's core? *Icarus*, *151*(1), 118–122. https://doi.org/10.1006/icar.2001.6586

Hauck, S. A., Margot, J.-L., Solomon, S. C., Phillips, R. J., Johnson, C. L., Lemoine, F. G., et al. (2013). The curious case of Mercury's internal structure. *Journal of Geophysical Research: Planets*, *118*(6), 1204–1220. https://doi.org/10.1002/jgre.20091

Hirao, N., Ohtani, E., Kondo, T., & Kikegawa, T. (2004). Equation of state of iron–silicon alloys to megabar pressure. *Physics and Chemistry of Minerals*, *31*(6), 329–336. https://doi.org/10.1007/s00269-004-0387-x

Kuskov, O. L., & Kronrod, V. A. (2001). Core sizes and internal structure of Earth's and Jupiter's Satellites. *Icarus*, *151*(2), 204–227. https://doi.org/10.1006/icar.2001.6611

Lai, X., Zhu, F., Zhang, J. S., Zhang, D., Tkachev, S., Prakapenka, V. B., & Chen, B. (2020). An externally-heated diamond anvil cell for synthesis and single-crystal elasticity determination of ice-VII at high pressure-temperature conditions. *Journal of Visualized Experiments*, *160*, e61389. https://doi.org/10.3791/61389

Laneuville, M., Wieczorek, M. A., Breuer, D., Aubert, J., Morard, G., & Rückriemen, T. (2014). A long-lived lunar dynamo powered by core crystallization. *Earth and Planetary Science Letters*, *401*, 251–260. https://doi.org/10.1016/j.epsl.2014.05.057

Lin, J.-F., Campbell, A. J., Heinz, D. L., & Shen, G. (2003). Static compression of iron-silicon alloys: Implications for silicon in the Earth's core. *Journal of Geophysical Research*, *108*(B1). https://doi.org/10.1029/2002JB001978

Lin, J.-F., Heinz, D. L., Campbell, A. J., Devine, J. M., & Shen, G. (2002). Iron-silicon alloy in Earth's core? *Science*, *295*(5553), 313–315. https://doi.org/10.1126/science.1066932

Matsuyama, I., Nimmo, F., Keane, J. T., Chan, N. H., Taylor, G. J., Wieczorek, M. A., et al. (2016). GRAIL, LLR, and LOLA constraints on the interior structure of the Moon. *Geophysical Research Letters*, *43*(16), 8365–8375. https://doi.org/10.1002/2016GL069952

Morgan, J. W., & Anders, E. (1980). Chemical composition of Earth, Venus, and Mercury. *Proceedings of the National Academy of Sciences*, *77*(12), 6973–6977. https://doi.org/10.1073/pnas.77.12.6973

Nakajima, Y., Kawaguchi, S. I., Hirose, K., Tateno, S., Kuwayama, Y., Sinmyo, R., et al. (2020). Silicon-depleted present-day Earth's outer core revealed by sound velocity measurements of liquid Fe-Si alloy. *Journal of Geophysical Research: Solid Earth*, *125*(6), e2020JB019399. https://doi.org/10.1029/2020JB019399

Nittler, L. R., Chabot, N. L., Grove, T. L., & Peplowski, P. N. (2017). The chemical composition of Mercury. In *Mercury: The view after MESSENGER*. Cambridge University Press. 1712.02187.

Numakura, K. I., Tsugawa, A., Sugano, M., & Sato, Y. (1972). Magnetic and electric properties of iron-silicon alloys. *Science Reports of the Research Institutes, Tohoku University - Series A: Physics, Chemistry, and Metallurgy*, *24*, 48–60.

Ohnuma, I., Abe, S., Shimenouchi, S., Omori, T., Kainuma, R., & Ishida, K. (2012). Experimental and thermodynamic studies of the Fe-Si binary system. *ISIJ International*, *52*(4), 540–548. https://doi.org/10.2355/isijinternational.52.540

Ouyang, G., Jensen, B., Macziewski, C. R., Ma, T., Meng, F., Lin, Q., et al. (2019). Characterization of ordering in Fe-6.5%Si alloy using X-ray, TEM, and magnetic TGA methods. *Materials Characterization*, *158*, 109973. https://doi.org/10.1016/j.matchar.2019.109973

Prescher, C., & Prakapenka, V. B. (2015). DIOPTAS: A program for reduction of two-dimensional X-ray diffraction data and data exploration. *High Pressure Research*, *35*(3), 223–230. https://doi.org/10.1080/08957959.2015.1059835

Sakairi, T., Ohtani, E., Kamada, S., Sakai, T., Sakamaki, T., & Hirao, N. (2017). Melting relations in the Fe–S–Si system at high pressure and temperature: Implications for the planetary core. *Progress in Earth and Planetary Science*, *4*(1), 10. https://doi.org/10.1186/s40645-017-0125-x

Secco, R. A. (2017). Thermal conductivity and Seebeck coefficient of Fe and Fe-Si alloys: Implications for variable Lorenz number. *Renewable Energy*, *113*. https://doi.org/10.1016/j.renene.2017.01.061

Seto, Y., Nishio-Hamane, D., Nagai, T., & Sata, N. (2010). Development of a software suite on X-ray diffraction experiments. *The Review of High Pressure Science and Technology*, *20*(3), 269–276. https://doi.org/10.4131/jshpreview.20.269

Shim, D. (2017). *Pytheos - A python tool set for equations of state*. Zenodo.

Steinbrügge, G., Dumberry, M., Rivoldini, A., Schubert, G., Cao, H., Schroeder, D. M., & Soderlund, K. M. (2021). Challenges on Mercury's interior structure posed by the New measurements of its obliquity and tides. *Geophysical Research Letters*, *48*(3), e2020GL089895. https://doi.org/10.1029/2020GL089895

Tateno, S., Kuwayama, Y., Hirose, K., & Ohishi, Y. (2015). The structure of Fe–Si alloy in Earth's inner core. *Earth and Planetary Science Letters*, *418*, 11–19. https://doi.org/10.1016/J.EPSL.2015.02.008

Terasaki, H., Rivoldini, A., Shimoyama, Y., Nishida, K., Urakawa, S., Maki, M., et al. (2019). Pressure and composition effects on sound velocity and density of core-forming liquids: Implication to core compositions of terrestrial planets. *Journal of Geophysical Research: Planets*, *124*(8), 2272–2293. https://doi.org/10.1029/2019JE005936

Tsujino, N., Nishihara, Y., Nakajima, Y., Takahashi, E., Funakoshi, K., & Higo, Y. (2013). Equation of state of γ-Fe: Reference density for planetary cores. *Earth and Planetary Science Letters*, *375*, 244–253. https://doi.org/10.1016/J.EPSL.2013.05.040

Van Hoolst, T., & Jacobs, C. (2003). Mercury's tides and interior structure. *Journal of Geophysical Research*, *108*(E11). https://doi.org/10.1029/2003JE002126

Van Hoolst, T., Sohl, F., Holin, I., Verhoeven, O., Dehant, V., & Spohn, T. (2007). Mercury's interior structure, rotation, and tides. *Space Science Reviews*, *132*(2–4), 203–227. https://doi.org/10.1007/S11214-007-9202-6/METRICS

Wang, B., Li, G., Wang, Y., Su, Y., Sun, H., Guo, Z., et al. (2021). Characterization of the Fe-6.5wt%Si strip with rapid cooling coupling deep supercooled solidification. *ACS Omega*, *6*(39), 25412–25420. https://doi.org/10.1021/acsomega.1c03367

Wang, S., Berrada, M., Chao, K. H., Lai, X., Zhu, F., Zhang, D., et al. (2023). Externally Heated Diamond ANvil Cell Experimentation (EH-DANCE) for studying materials and processes under extreme conditions. *Review of Scientific Instruments*, *94*(12), 123902. https://doi.org/10.1063/5.0180103

Weber, R. C., Lin, P.-Y., Garnero, E. J., Williams, Q., & Lognonné, P. (2011). Seismic detection of the lunar core. *Science*, *331*(6015), 309–312. https://doi.org/10.1126/science.1199375

Wieczorek, M. A., Jolliff, B. L., Khan, A., Pritchard, M. E., Weiss, B. P., Williams, J. G., et al. (2006). The constitution and structure of the lunar interior. *Reviews in Mineralogy and Geochemistry*, *60*(1), 221–364. https://doi.org/10.2138/rmg.2006.60.3

Williams, J. G., Konopliv, A. S., Boggs, D. H., Park, R. S., Yuan, D.-N., Lemoine, F. G., et al. (2014). Lunar interior properties from the GRAIL mission. *Journal of Geophysical Research: Planets*, *119*(7), 1546–1578. https://doi.org/10.1002/2013JE004559

Yokoo, S., Edmund, E., Morard, G., Anna Baron, M., Boccato, S., Decremps, F., et al. (2023). Composition-dependent thermal equation of state of B2 Fe-Si alloys at high pressure. *American Mineralogist*, *108*(3), 536–542. https://doi.org/10.2138/AM-2022-8067

Zhang, J., & Guyot, F. (1999). Thermal equation of state of iron and $Fe_{0.91}Si_{0.09}$. *Physics and Chemistry of Minerals*, *26*(3), 206–211. https://doi.org/10.1007/s002690050178